

## Development of an integrated needle insertion system with image guidance and deformation simulation

Yo Kobayashi<sup>a,\*</sup>, Akinori Onishi<sup>b</sup>, Hiroki Watanabe<sup>b</sup>, Takeharu Hoshi<sup>b</sup>, Kazuya Kawamura<sup>a</sup>, Makoto Hashizume<sup>c</sup>, Masakatsu G. Fujie<sup>a</sup>

<sup>a</sup> Faculty of Science and Engineering, Waseda University, Japan

<sup>b</sup> Graduate School of Science and Engineering, Waseda University, Japan

<sup>c</sup> Center for the Integration of Advanced Medicine and Innovative Technology, Kyushu University Hospital, Japan

### ARTICLE INFO

#### Article history:

Received 31 January 2009

Received in revised form 21 August 2009

Accepted 24 August 2009

#### Keywords:

Needle insertion

Image guidance

Deformation simulation

Surgical robot

Physical model

Viscoelastic and nonlinear properties

Liver

### ABSTRACT

**Objective:** The purpose of our work was to develop an integrated system with image guidance and deformation simulation for the purpose of accurate needle insertion.

**Methods:** We designed an ultrasound-guided needle insertion manipulator and physical model to simulate liver deformation. We carried out an in vivo experiment using a porcine liver to verify the effectiveness of our manipulator and model.

**Results:** The results of the in vivo experiment showed that the needle insertion manipulator accurately positions the needle tip into the target. The experimental results also showed that the liver model accurately reproduces the nonlinear increase of force upon the needle during insertion.

**Discussion:** Based on these results, it is suggested that the needle insertion manipulator and the physical liver model developed and validated in this work are effective for accurate needle insertion.

© 2009 Elsevier Ltd. All rights reserved.

## 1. Introduction

As a cancer treatment method, percutaneous therapy is now a focus of attention. For example, percutaneous ethanol injection therapy (PEIT) and radio frequency ablation (RFA) are performed for liver cancer. In this form of treatment, cancer cells existing inside the organ are necrotized by the delivery of a needle tip that injects either ethanol (PEIT) or ablates (RFA). Percutaneous therapy has become a major trend in liver cancer treatment because it is very minimally invasive but achieves sufficient results [1,2].

Medical procedures such as PEIT and RFA require the insertion of a needle into a specific part of the diseased area. In all cases, the needle tip should be as close as possible to the center of the target cancer. In recent years, research and development has been carried out on surgical robots and navigation systems for minimally invasive and precise surgery [3,4]. Research into robotic systems to assist needle insertion has also been conducted to improve the accuracy of needle placement and expansion of the approach path [5,6].

However, there is a remaining large problem in regard to accurate needle insertion: organ deformation. The needle insertion site, in the case of the liver for example, is very soft, and it is easy for the force of the needle to deform the tissues and, as a result, for the position of the target cancer to be displaced. Therefore, when the needle is inserted, there is a corresponding risk of organ deformation and the resulting target cancer displacement. Therefore, it is necessary to take organ deformation into account and make a plan for insertion position and orientation that will allow the manipulator to guide the needle tip to the displaced cancer. To make this plan, a simulation method in a virtual surgery environment reproduced with physical models of organs may be used to predict and visualize the organ deformation. The purpose of our study was to use such a method and develop an integrated robotic system with image guidance and deformation simulation for the purpose of accurate needle insertion.

### 1.1. Needle insertion manipulator

There can be some problems when surgeons manually insert needles, including different treatment results and the possibility of a complicating disease resulting from needle insertion into large blood vessels, etc. The purpose for developing a needle insertion robot is to realize accurate needle insertion independent of surgeon skills.

\* Corresponding author. Tel.: +81 3 5286 3412; fax: +81 3 5291 8269.  
E-mail address: [you-k@aoni.waseda.jp](mailto:you-k@aoni.waseda.jp) (Y. Kobayashi).

Various types of robotic systems to assist with needle insertion have been researched [7–19]. Masamune and Fichtinger et al. have investigated a robotic system guided by images from a CT scanner inside a gantry [7,8]. Loser et al. have developed a needle insertion system in which the needle position is controlled using the image of CT fluoroscopy [9]. Yanof et al. have researched a CT-guided robot for interventional procedures with preoperative and intraoperative planning [10].

Many researchers have also developed MRI-guided needle insertion manipulators [11–15]. Masamune et al. have developed a small robot system in which an MRI machine controls needle orientation in a narrow gantry space [11]. Hashizume et al. have developed an MR image-guided surgical robotic system for minimally invasive laparoscopic surgery, including needle insertion manipulator [12]. Krieger et al. have developed a remotely actuated manipulator for access to prostate tissue under MR imaging guidance [13]. Tajima et al. have developed an MRI-compatible manipulator for heart surgery [14]. And, our group also has developed an MRI-compatible needle insertion manipulator with a bending joint inside organ [15].

Ultrasound-guided needle insertion manipulators also have been developed [16–19]. Hong et al. have researched an ultrasound-guided needle insertion robot for percutaneous cholecystostomy [16]. Fichtinger et al. have researched a robot-assisted prostate brachytherapy system based on transrectal ultrasound [17]. Terayama et al. have researched a needle insertion system that uses a curved multi-tube device [18]. Finally, Corral et al. have researched an automatic needle-placement robot for needle insertion into the spine [19].

We have used ultrasound equipment in this research to visualize the position of the target cancer, and ultrasound images guided operation of the needle insertion manipulator. The ultrasound images usually are used in the needle insertion process because ultrasound equipment provides real-time imaging of internal organs and is easily set up. In addition, compared with CT and MRI equipment, ultrasound equipment is in more widespread use.

The needle insertion manipulator itself must be compact, so that it does not interfere with the surgeon's access to the patient during an operation. In addition, the manipulator must position the tip of the needle accurately. However, the ultrasound-guided needle insertion manipulators in related work are somewhat large, while these manipulator realized accurate positioning of needle tip. Then, our work focused on the development of a compact needle insertion system. Our design for an integrated needle insertion manipulator with an ultrasound probe realized to be compact. It should be noted that Hong et al. already have developed an integrated needle insertion manipulator with two degrees of freedom [16], while our manipulator has three degree of freedom. This additional degree of freedom increases the flexibility of the approach path and the likeliness of avoiding large blood vessels. In addition, the novel power-transmission system we proposed, provide that the manipulator system was more compact than the related work.

## 1.2. Organ modeling

Physical organ modeling recently has aroused considerable attention, [20–33]. For example, the Physiome Project is known worldwide [21]. In addition, Miller et al. have presented three-dimensional, nonlinear, viscoelastic constitutive models for the liver and kidney [22], and for brain tissue [23]. Conventional research into the modeling of living bodies mainly concerns deformation analysis using a finite element method (FEM) for surgical simulation and training. For example, Tiller et al. have developed a deformation analysis of the uterus using FEM [24]. Alterovitz et

al. have studied the simulation of needle insertion for prostate brachytherapy [25,26]. Meanwhile, DiMaio and Salcudean have used a linear elastic material model to illustrate a system for measuring the extent of planar tissue phantom deformation during needle insertion [27,28]. Moreover, Sakuma et al. have created an equation that combines both logarithmic and polynomial strain energy forms of a porcine liver from combined compression and elongation tests [29,30]. Salcudean et al. have designed a planning system to determine the optimized insertion angle and position using a linear and nonlinear organ model [31,32]. Finally, Schwartz et al. have presented a viscoelastic and nonlinear model for the simulation of needle insertion [33].

In general, organ tissue is inhomogeneous and exhibits nonlinear, anisotropic elastic and viscous behavior [20]. In particular, viscoelastic and nonlinear properties are important for precise needle insertion into the liver because of following reasons; the nonlinear properties affect the response of liver deformation when there is a large deformation [34], while the viscoelastic properties affect the dependence of liver deformation on insertion velocity [35]. Thus, an accurate liver model, including viscoelastic and nonlinear properties, is required for precise needle insertion.

Our work focused on the development of a model, including both viscoelastic and nonlinear properties, for the simulation of needle insertion. Schwartz et al. already have presented a model including viscoelastic and nonlinear properties [33]. However, the material properties included in that model are only coarse approximations of the real material properties of biological soft tissues while the model can simulate deformation at speeds which are compatible with real-time applications. It means that the material model was not constructed referring to the measured material data from real tissues. The originality of our modeling was to measure the detailed material properties of real liver tissues about viscoelasticity and nonlinearity. We have also developed FEM-based liver model using the measured material properties and simulated the liver deformation during needle insertion [36–40].

## 1.3. Objectives

The objectives of our work were to develop an integrated robotic system with an image-guided needle insertion manipulator and also a deformation simulation system using a physical model of a liver for the path planning of needle insertion. This paper presents our ultrasound-guided needle insertion manipulator and physical model to simulate liver deformation. We also discuss the in vivo experiment we conducted to verify the effectiveness of our needle insertion manipulator and liver model.

We developed 2D liver model and provided the 2D deformation simulation in this paper while a 3D model would provide more accurate results. The manipulator movement we developed is also limited in 2D plane of ultrasound image. It is assumed that 2D simulation and manipulator movement is enough effective to realize the accurate needle insertion because the surgeon usually insert the needle using only 2D ultrasound images. In addition, the 2D model is possible to be used intraoperatively while 3D deformation simulation brings a potentially vast increase in the calculation time required.

The rest of this paper is organized as follows: Section 2 presents the development of our ultrasound-guided needle insertion manipulator. Section 3 discusses the development of our liver model, including the material properties of the model and the formulation and solution of the FEM-based model. Section 4 discusses the methodology of our in vivo validation experiment and its results. Finally, Section 5 presents a summary, overall conclusions, and a look at future work.

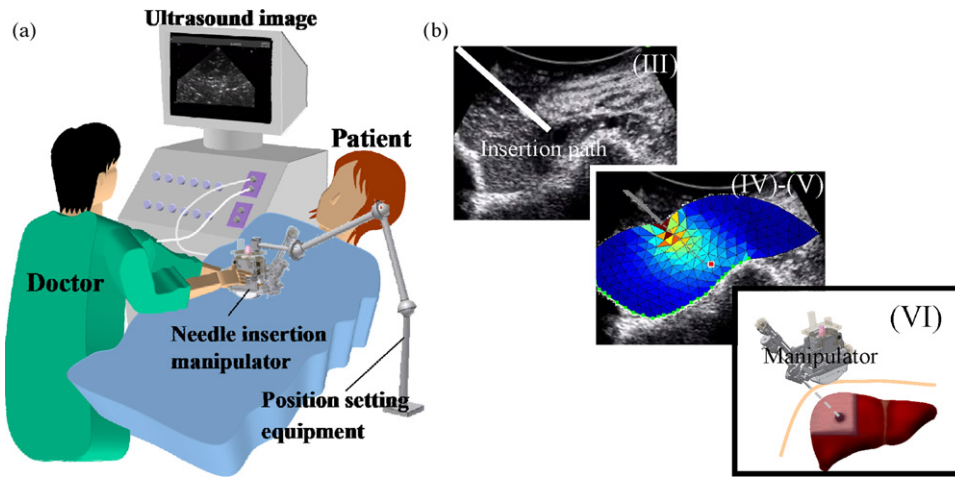


Fig. 1. The process of treatment using the integrated needle insertion manipulator. (a) process (I)–(II) and (b) process (III)–(VI).

## 2. Ultrasound-guided needle insertion manipulator

### 2.1. Design and operational concepts

Our design for an integrated needle insertion manipulator with an ultrasound probe provides compactness and high-accuracy positioning, because it decreases registration error. The process of treatment using the integrated needle insertion manipulator is as follows (Fig. 1):

- (I) The needle insertion manipulator is combined to the position setting equipment such as endoscope holding device. 3D position of the manipulator is flexibly changed and fixed at any position by the device.
- (II) The surgeon moves the ultrasound probe by hand and scans the target cancer. Surgeon set the ultrasound probe with needle insertion manipulator at an adequate position to visualize the target cancer in ultrasound image. In this process, the navigation system to present the position of ultrasound probe and tumor, which is reported in such as [41], is useful for the surgeon to set the probe. We will integrate such navigation system near future.
- (III) Needle insertion position and orientation are decided by the surgeon from the position of the target cancer displayed in the ultrasound images. In this process, the surgeon then uses the GUI (Graphical User Interface) to order the needle insertion path from the computer.
- (IV) The position of the ultrasound probe with needle insertion manipulator is obtained using an optical 3D position measurement system. Then, the position is registered to the preoperative CT or MRI diagnostic image of liver. We do not integrate this registration process into our system. The registration technique reported in such as [41] will be used near future.

- (V) The physical liver model is developed based on the obtained images. Then, deformation of the liver during needle insertion is simulated. The surgeon optimizes insertion path using the simulation results of deformation (see Section 3)
- (VI) The position of the needle is set at the insertion path determined in (V) by the manipulator. The needle is inserted into the target cancer.

### 2.2. Power transmission

The manipulator tends to be large when the actuator is included in the manipulator itself. Then, to keep the manipulator compact, the actuator should be outside the manipulator, positioned in such a way that it still can effectively transmit power to the manipulator. Since the actuator is positioned at a distance from the manipulator, it also is at a distance from the patient, which increases safety. We used a power-transmission system called a “Flexible Rack” in our development of the needle insertion manipulator. Fig. 2 presents the flexible rack and guide tube. Since the rack is made from flexible material, it bends easily and provides power transmission via a flexible path, whereas a rack made from metal provides only a straight pass. The flexible rack is moved inside a guide tube to avoid rack deflection and interference with other parts of the system.

At times, however, the rack does deflect and buckle, which causes lost motion ( $L_1 - L_0$  in Fig. 3) and, in turn, a loss in power and accuracy. So, to ensure accurate movement, a method to respond to the lost motion is required. Fig. 3 displays the power-transmission mechanism that we developed. The flexible rack is pushed and pulled when the input pinion gear (pinion 1) is rotated by the input actuator. The rack then rotates the output pinion gear (pinion 2). The output pinion gear is coupled to the shaft of a ball screw, and the flange of the ball screw is translated by the rotation of the ball screw. The translation of the flange is used as the output for manipulator movement.

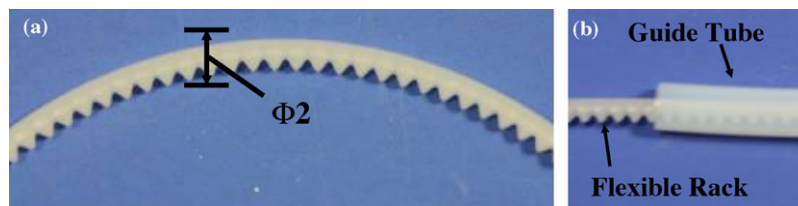
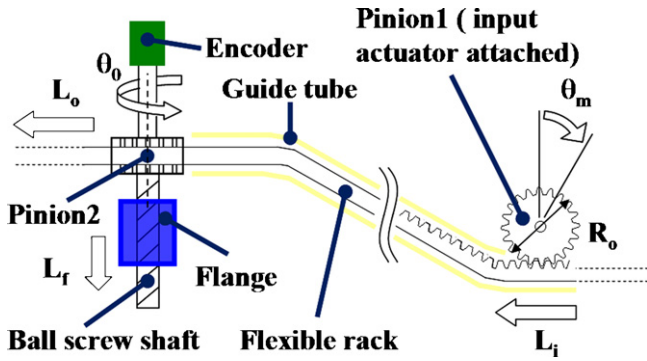


Fig. 2. Flexible-rack system. (a) Flexible rack and (b) flexible rack inside guide tube. The flexible rack bends easily and provides power transmission via a flexible path since the rack is made from flexible material. The flexible rack is moved inside a guide tube to avoid rack deflection and interference with other parts of the system.



**Fig. 3.** Mechanism of power transmission. The flexible rack is pushed and pulled when the input pinion gear (pinion 1) is rotated by the input actuator. The rack then rotates the output pinion gear (pinion 2). The output pinion gear is coupled to the shaft of a ball screw, and the flange of the ball screw is translated by the rotation of the ball screw. The translation of the flange is used as the output for manipulator movement.

The following actions are countermeasures to the lost motion: (1) sensing the output rotational movement  $\theta_o$ , (2) reducing this movement, and (3) increasing the low back drivability of this movement. In regard to (1), the rotation of the output pinion gear is measured by the encoder attached to the shaft of the ball screw.

The position of output flange  $L_f$  is controlled using this information. In regard to action (2), the ball screw part reduces the movement  $L_o$  at the output part to the translation of the flange  $L_f$ . The ball screw part has the low back drivability (3). It realizes to cut off the external force to the flexible rack, which is easily moved by an external force. In short, this power-transmission system achieves accurate positioning independent of lost motion.

### 2.3. Manipulator mechanism

The developed manipulator is shown in Fig. 4. Fig. 4(a) is the translation side, and Fig. 4(b) is the slide-crank side. Our manipulator has three degrees of freedom (DOF). Fig. 5(a) is a mechanical outline drawing of our manipulator mechanism, while Fig. 5(b) displays the composition of the DOFs of our manipulator. One DOF is for “(A) horizontal positioning”, which decides the position of the manipulator horizontal direction in relation to the cross-section of the ultrasound image. One DOF is for “(B) posture”, which decides the needle insertion angle. Another DOF is for “(C) needle insertion”, which decides needle insertion after the needle position and angle have been determined.

All DOFs of the manipulator are moved by the translation movement generated by the flexible-rack power-transmission system. Fig. 6 displays link mechanism to realize each DOF. The DOF of (A) horizontal positioning is moved when both translations (I) and (II)

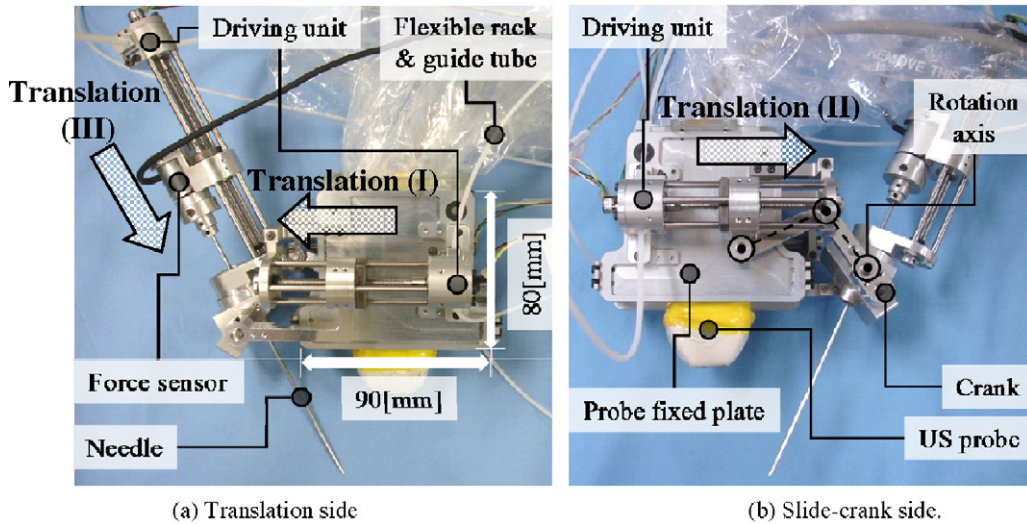


**Fig. 4.** Overview of manipulator: (a) is the translation side, and (b) is the slide-crank side. This manipulator has three degrees of freedom (DOF). A six-axis force sensor is installed in the needle insertion unit. The accuracy of this manipulator is about 0.1 mm. (a) Translation side and (b) slide-crank side.

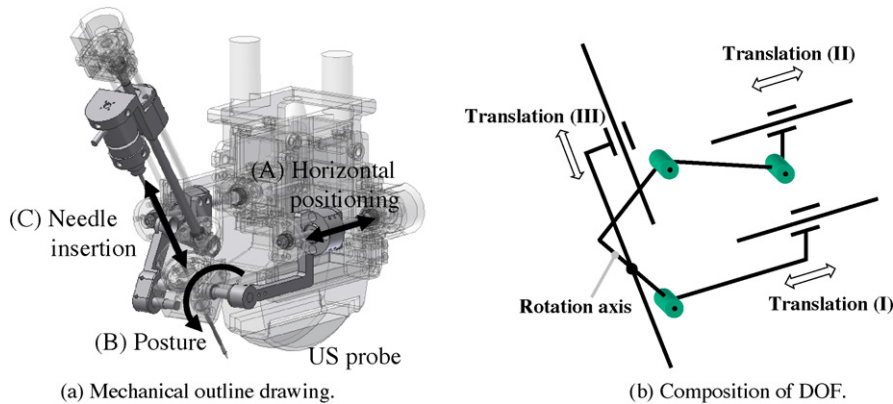


**Fig. 5.** Mechanism of manipulator. All DOFs of the manipulator are moved by the translation movement (I)–(III) generated by the flexible-rack power-transmission system. (a) Mechanical outline drawing and (b) composition of DOF.



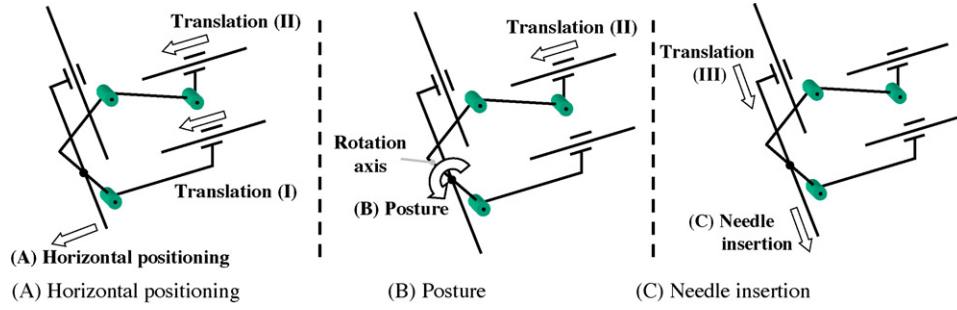


**Fig. 6.** Link mechanism to realize each DOF. The DOF of (A) horizontal positioning is moved when both translations (I) and (II) are driven by the same displacement. The DOF of (B) posture is changed only when translation (II) is displaced while translation (I) is fixed. The DOF of (C) needle insertion is driven by translation (III). (A) Horizontal positioning, (B) posture and (C) needle insertion.

are driven by the same displacement. The DOF of (B) Posture is changed only when translation (II) is displaced while translation (I) is fixed. In this situation, the translation movement generated by the flexible-rack power-transmission system is changed to rotation movement using the slider-crank mechanism to set the posture of the needle. The DOF of (C) Needle insertion is driven by translation (III); the needle is attached to the unit of translation (III), and it is moved in the axial direction.

The range of movement of each DOF is decided in response to various positions of the target cancer in both shallow and deep locations in the liver. (A) Horizontal positioning has a 40-mm translation of movement, (B) Posture has a  $\pm 30^\circ$  range of movement, and (C) Needle insertion has a 60-mm translation of movement. A six-axis force sensor is installed in the needle insertion unit, and the force information loaded on the needle is measured by the sensor. The manipulator, which is designed to hold various sizes of conventional ultrasound probes, is 80 mm high  $\times$  90 mm wide  $\times$  44 mm deep, which is a handy size for use in operations. The positioning accuracy of this manipulator is about 0.1 mm from the result of experiment using 3D position measurement system, which has about 0.1 mm accuracy.

### 3. Deformation simulation of liver

Our work focused on the development of a model, including both viscoelastic and nonlinear properties, for the simulation of needle insertion. A porcine liver was used as the sample for this study because porcine organs have frequently been used as a substitute for human organs due to their similarity [29,34].

#### 3.1. Material properties

We already have reported the material properties of a porcine liver in [36,37], and these papers also gave specific descriptions of the physical properties of the liver. Thus, only a simplified explanation of the material behavior used for deformation calculation is shown in this paper. Experiments were individually implemented to measure the physical properties of the porcine's interior liver using a rheometer (TA-Instrument: AR550). The shear modulus, shear stress, and shear strain were then calculated based on these results.

##### 3.1.1. Viscoelastic properties

A dynamic viscoelastic test was carried out to measure the frequency response of the liver. A sine-wave stress from 0.1 to 10 rad/s, providing 3% strain amplitude, was loaded on the liver, and a dynamic viscoelastic test was conducted. The mechanical impedance of the porcine liver obtained from the result of this test is shown in Fig. 7. The needle is generally inserted into the organ at a low velocity; hence the response is mainly affected by

the low frequency characteristics. Thus, we used the viscoelastic model using the fractional derivative described in (1), which takes only low-frequency characteristics into consideration.

$$G \frac{d^k \gamma}{dt^k} = \tau \quad (1)$$

where  $G$  is the viscoelasticity,  $k$  is the order of derivative,  $\gamma$  is the shear strain,  $\tau$  is the shear stress and  $t$  is time. The derivative order  $k$  was approximately equal to 0.1, based on the slopes of  $G'$  and  $G''$  shown in Fig. 7.

##### 3.1.2. Nonlinear properties (strain dependence of elastic modulus)

The nonlinear characteristics of liver as a material were investigated based on the creep test, in which the step response is measured. The steady state of the step response following sufficient elapsed time exhibits the low-frequency characteristics described in (1). Eq. (1) becomes (2) if (1) is solved by the condition of the creep test.

$$\gamma = \frac{\tau_c}{G\Gamma(1+k)} t^k = \gamma_c t^k \quad (2)$$

where  $\tau_c$  is constant shear stress,  $\Gamma()$  is the gamma function, and  $\gamma_c$  is the coefficient deciding the strain value.

The creep test for each stress was carried out repeatedly while the viscoelasticity  $G$  and strain  $\gamma_c$  for each stress were calculated using (2). From these results, the graph in Fig. 8 shows the dependence of viscoelasticity  $G$  on strain  $\gamma_c$ . A liver with a low strain of less than about 0.35 displays linear characteristics and a viscoelasticity  $G$  at a constant 400 Pa. A liver with a high strain of more than about

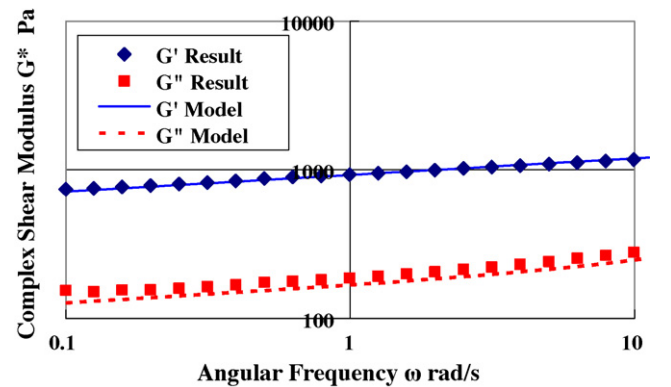


**Fig. 7.** Mechanical impedance of liver. This figure shows the experimental result of dynamic viscoelastic test.  $G^*$  is a complex shear modulus,  $G'$  is a storage elastic modulus, and  $G''$  is a loss elastic modulus.  $G$  and  $G'$  increase proportionally in the log-log diagram. Then, we used the viscoelastic model using the fractional derivative described in (1). This model accurately fit the experimental result as shown in this figure.

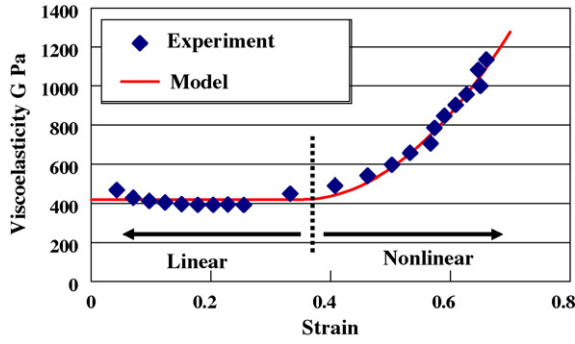


**Fig. 8.** Strain dependence of viscoelasticity  $G$ . This result was obtained from the creep test for each stress. A liver with a low strain displays linear characteristics, while a liver with a high strain displays nonlinear characteristics. Then, the strain dependence of viscoelasticity was modeled using the quadratic function of strain shown in (3).

0.35 displays nonlinear characteristics and an increased degree of viscoelasticity  $G$ . Then, the strain dependence of viscoelasticity was modeled using the quadratic function of strain shown in (3):

$$G(\gamma) = \begin{cases} G_0 & (\gamma < \gamma_0) \\ G_0(1 + \alpha_\gamma(\gamma - \gamma_0)^2) & (\gamma > \gamma_0) \end{cases} \quad (3)$$

where  $G_0$  is the viscoelastic modulus of the strain slope between 0 and 0.35 in Fig. 8.  $\alpha_\gamma$  is the coefficient deciding the change of stiffness, and  $\gamma_0$  is the strain at which the characteristics of the liver change to show nonlinearity.

### 3.1.3. Shear stress–strain relation

The material properties of the liver were modeled using (4) from the discussion in Sections 3.1.1 and 3.1.2.

$$G(\gamma) \frac{d^k \gamma}{dt^k} = \tau \quad (4)$$

### 3.1.4. Stress–strain relation

In general, the elastic modulus  $E$  was used to construct the deformation model. The relation between the elastic modulus  $E$  and the shear modulus  $G$  was calculated using Poisson's ratio  $\nu$  as in the following equation:

$$E = 2(1 + \nu)G \quad (5)$$

In the experiment using the rheometer, only the shear modulus was loaded on the test material. However, in the situation of deformation simulation, the stress state is more complex because it has more moduli. We assumed that the nonlinearity of the elastic modulus would be decided by the relative strain calculated in (6).

$$\varepsilon_r = \sqrt{\frac{1}{2} \{(\varepsilon_1 - \varepsilon_2)^2 + (\varepsilon_2 - \varepsilon_3)^2 + (\varepsilon_3 - \varepsilon_1)^2\}} \quad (6)$$

where  $E$  is the elastic modulus,  $\nu$  is Poisson's ratio,  $\varepsilon_r$  is relative strain,  $\varepsilon_1$ ,  $\varepsilon_2$ , and  $\varepsilon_3$  are the principal strains.

Thus, from these considerations, the material properties using the liver model can be described in (7) and (8).

$$E(\varepsilon_r) \frac{d^k \varepsilon}{dt^k} = \sigma \quad (7)$$

$$E(\varepsilon_r) = \begin{cases} E_0 & (\varepsilon_r < \varepsilon_0) \\ E_0(1 + \alpha_\varepsilon(\varepsilon_r - \varepsilon_0)^2) & (\varepsilon_r > \varepsilon_0) \end{cases} \quad (8)$$

where  $E(\varepsilon_r)$  is nonlinear elastic modulus,  $\varepsilon_r$  is relative strain,  $\varepsilon$  is strain,  $\sigma$  is stress,  $E_0$  is the elastic modulus between linear range,  $\alpha_\varepsilon$  is the coefficient deciding the change of stiffness, and  $\varepsilon_0$  is the strain at which the characteristics of the liver change to show nonlinearity.

### 3.2. FEM-based modeling

This section shows the formulation of the FEM model using the material properties described in Section 3.1. Since we already have given specific descriptions in this regard [38,39], the following will be only a simplified explanation.

The expressions between the displacements at all the nodal points and all the applied loads are shown in (9)–(11), from the result of (8).

$$\mathbf{K}(\mathbf{U}) D^{(k)} \mathbf{U} = \mathbf{F} \quad (9)$$

where  $\mathbf{F}$  is external force vector,  $\mathbf{K}(\mathbf{U})$  is nonlinear overall stiffness matrix,  $\mathbf{U}$  is overall displacement (deformation) vector, and  $D^{(k)}$  means  $k$ th-order derivative.

$$\mathbf{K}(\mathbf{U}) = \sum_{\text{all elements}} \mathbf{k}(\varepsilon_r) \quad (10)$$

$$\mathbf{k}(\varepsilon_r) = \begin{cases} \mathbf{k}_0 & (\varepsilon_r < \varepsilon_0) \\ \mathbf{k}_0(1 + \alpha_\varepsilon(\varepsilon_r - \varepsilon_0)^2) & (\varepsilon_r > \varepsilon_0) \end{cases} \quad (11)$$

where  $\mathbf{k}$  is the nonlinear element stiffness matrix,  $\mathbf{k}_0$  is the element stiffness matrix when the liver tissue shows linear characteristics,  $\alpha_\varepsilon$  is the coefficient deciding the change of stiffness, and  $\varepsilon_r$  is the relative strain.

First, the solution for the viscoelastic system is shown in Section 3.2.1, and the solution for the nonlinear system is given in Section 3.2.2. Finally, the solution for (9) is shown based on the discussions from both Sections 3.2.1 and 3.2.2.

#### 3.2.1. Solution for the viscoelastic system

The analysis can be considerably simplified when the following conditions are fulfilled [42]:

- The derivative operator of (9) is a common factor in all element stiffness.
- Only the external loads influence the stresses.

Then, Eq. (12) is derived from (9).

$$\mathbf{K}(\mathbf{U}) \mathbf{U} = \mathbf{F}' (\mathbf{F}' = D^{(-k)} \mathbf{F}) \quad (12)$$

where  $D^{(-k)}$  is the  $k$ th-order integration.

Eq. (12) is identical to the elastic problem when the virtual external force vector  $\mathbf{F}'$  is used. The fractional calculation (12) for each component of the external force vector  $\mathbf{F}$  was implemented to obtain the virtual external force vector  $\mathbf{F}'$ . We used the sampling time scaling property introduced in [43] to make a discrete fractional calculation. We used the sampling time scaling property to consider the discrete fractional order integrals as the “deformation” of their integer order counterparts.

#### 3.2.2. Nonlinear system

Incremental approaches are important to obtain a significant answer, because the answer is not unique for many nonlinear situations. The incremental form of a discrete nonlinear model is generally written as in (13).

$$\mathbf{K}_t(\mathbf{U}_n) \Delta \mathbf{U}_n = \Delta \mathbf{F}_n \quad (13)$$

where  $\mathbf{n}$  is step of calculation,  $\mathbf{K}_t$  is the tangential stiffness matrix,  $\mathbf{U}_n$  is the overall displacement vector,  $\Delta \mathbf{U}_n$  is an increment of the overall displacement vector, and  $\Delta \mathbf{F}_n$  is an increment of the overall external force. The tangential matrix  $\mathbf{K}_t$  is described by (14) from Eq. (11).

$$\mathbf{K}_t(\mathbf{U}) = \sum_{\text{all elements}} \mathbf{k}_t(\varepsilon_r) \quad (14)$$

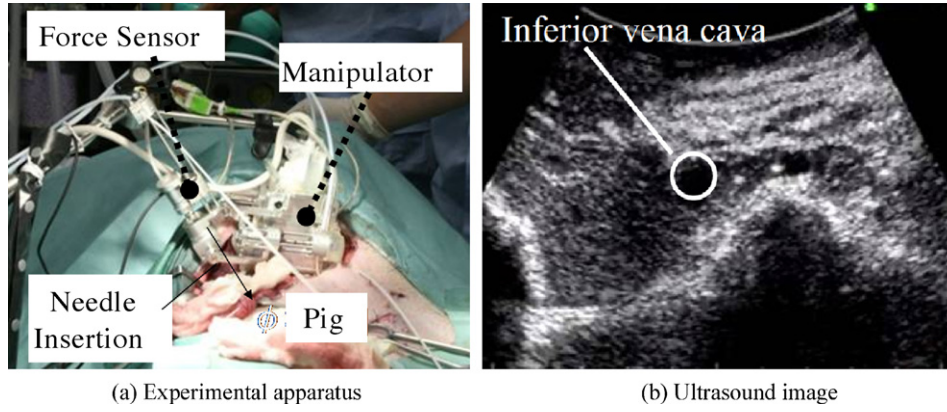


**Fig. 9.** Experimental setup of in vivo experiment. The inferior vena cava of the liver was chosen as the virtual target of the experiment. The needle insertion manipulator with ultrasound probe was set using the endoscope holding device at the location to visualize the target inferior vena cava in the ultrasound image. Then, the surgeon ordered the needle insertion path from the computer. The needle was inserted into the porcine liver at a constant speed of 5 mm/s from the path. (a) Experimental apparatus and (b) ultrasound image.

$$\mathbf{k}_t(\varepsilon_r) = \begin{cases} \mathbf{k}_0 & (\varepsilon_r < \varepsilon_0) \\ [1 + a_\varepsilon(\varepsilon_r - \varepsilon_0)^2 + 2a_\varepsilon(\varepsilon_r - \varepsilon_0)\varepsilon_r]\mathbf{k}_0 & (\varepsilon_r > \varepsilon_0) \end{cases} \quad (15)$$

We used both the Euler method and the modified Newton–Raphson method to solve the nonlinear system.

### 3.2.3. Calculation process

Based on these discussions, the solution for the system of (9) can be described as follows. First, the virtual external force  $\mathbf{F}'$  was calculated; then the incremental of  $\mathbf{F}'$  ( $\Delta\mathbf{F}'$ ) was computed. The solution to the nonlinear system described in Section 3.2.2 was then carried out using  $\Delta\mathbf{F}'$ .

$$\mathbf{K}_t(\mathbf{U}_n)\Delta\mathbf{U}_n = \Delta\mathbf{F}'_n \quad (16)$$

where  $\mathbf{n}$  is step of calculation,  $\mathbf{K}_t$  is the tangential stiffness matrix,  $\mathbf{U}_n$  is the overall displacement vector,  $\Delta\mathbf{U}_n$  is an increment of the overall displacement vector, and  $\Delta\mathbf{F}'_n$  is an increment of the virtual external force.

## 4. Validation experiment

### 4.1. Overview

This section shows the in vivo experimental validation of our needle insertion manipulator and physical liver model. The needle insertion experiment was carried out on a live porcine liver. The deformation of this liver was obtained from ultrasound images, while the deformation of the liver model was simulated by the computer program. By comparing the relations between needle displacement and force on the real liver and those in the liver model, we also were able to evaluate the model.

The following experiment in Section 4.2.1 is the same as the experiment described in our previous paper [40]. This paper presents the validation using the model with porcine liver shape, while the liver model in [40] was validated with the assumed that the liver was rectangle shape.

### 4.2. Methods

#### 4.2.1. In vivo experiment

Because a healthy porcine was used in the experiment, the inferior vena cava of the liver was chosen as the virtual target of the experiment. An inferior vena cava of a liver is clearly visible by ultrasound image and it is easy to confirm the phenomenon during needle insertion. Fig. 9 shows the experimental setup of the in vivo experiment. First, the surgeon searched the target inferior

vena cava by manipulating the ultrasound probe attached to the needle insertion manipulator. Next, the surgeon fixed the probe with the needle insertion manipulator using the endoscope holding device at the location to visualize the target inferior vena cava in the ultrasound image. Then, the surgeon then used the graphical user interface (GUI) to order the needle insertion path from the computer. Then, the needle was inserted into the porcine liver at a constant speed of 5 mm/s from the path, the ultrasound image was captured, and the force of the tissues against the needle was measured from force-sensor data.

#### 4.2.2. Analysis using liver model

To create the shape of the liver model, we used MRI image of porcine liver (Fig. 10). We have not yet integrated the registration technique with preoperative shape image of liver such as described in Section 2.1, so we used the MRI image obtained from other porcine in preliminary experiment. It means that the size of liver model was fit to the real liver while the shape was decided referring to MRI image of other porcine liver shown in Fig. 10. Therefore, this validation experiment was not rigorous, because the shape of a real porcine liver used in this experiment was not exactly the same as that of porcine liver of MRI image. A more-detailed analysis and

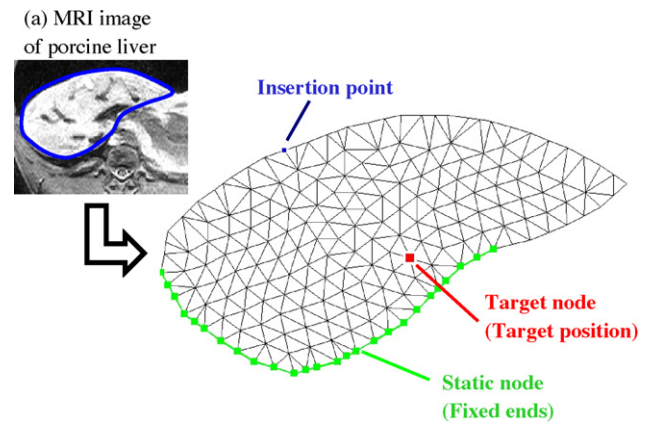


**Fig. 10.** Physical model of porcine liver. (a) MRI image and (b) physical model. We used MRI image of porcine liver to create the shape of the liver model. Applying Delaunay's method to the extracted outline data, a FEM mesh was created for use in the computer simulation. The green-colored nodes represent the fixed ends, taking into consideration rib and spine restrictions at the dorsal aspect of the abdomen, and the red node identifies the target position. The liver was assessed as though it were uniform.



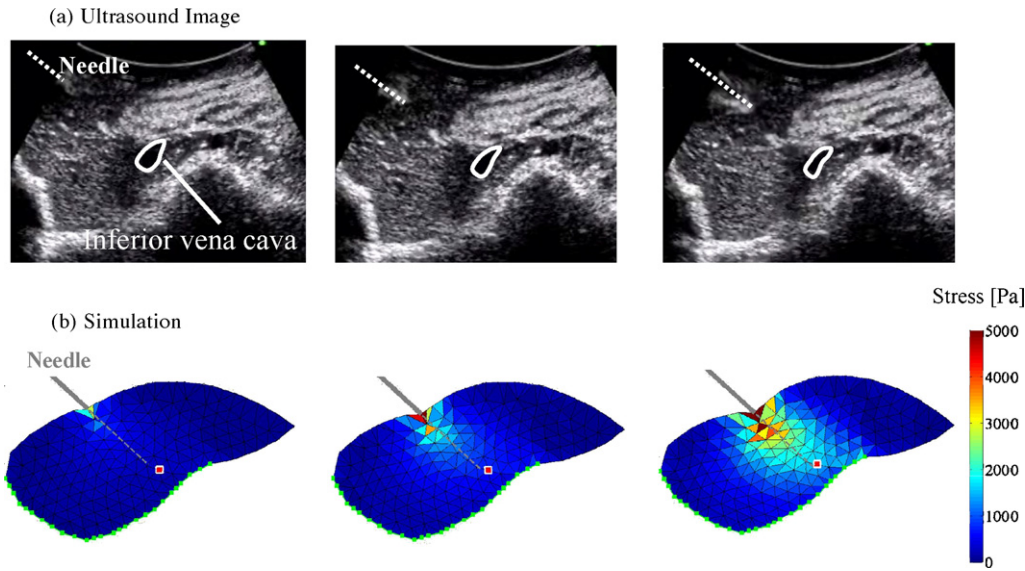


**Fig. 11.** Deformation of liver tissue by needle insertion. (a) As shown in ultrasound images and (b) as shown in simulation. The inferior vena cava in the liver collapsed from the force put on the needle by the liver tissues during insertion. (b) Shows a simulation of the deformation of the liver, which is confirmed by the ultrasound images captured during the experiment. In (b), the color of each finite element indicates the stress on it.

evaluation of the liver model with the real shape of a porcine liver used in the experiment should be carried out in future.

The images were outlined, and the outlines were manually extracted. Applying Delaunay's method to the extracted outline data, a FEM mesh was created for use in the computer simulation (Fig. 10). In Fig. 10, the green-colored nodes represent the fixed ends, taking into consideration rib and spine restrictions at the dorsal aspect of the abdomen, and the red node identifies the target position.

It also should be noted that the liver was assessed as though it were uniform, whereas an actual liver is made up of non-uniform tissue that even can include cirrhosis and cancer cells. The stiffness parameters, such as  $E_0$ ,  $\varepsilon_0$  and  $\alpha_\varepsilon$ , of the normal tissue were set manually to fit the measured data of needle insertion force. There also are large differences between the stiffness parameters of the in vitro liver and the in vivo liver. It is said that the in vivo liver is harder than the in vitro liver. It is assumed in our modeling that the viscoelastic and nonlinear properties of in vitro liver and in vivo liver can be represented using same Eq. (4) and only stiffness parameter such as  $E_0$ ,  $\varepsilon_0$  and  $\alpha_\varepsilon$ , are different between in vitro liver and in vivo liver.

The needle was assumed to be inserted at a constant speed of 5 mm/s. The time-series data of needle displacement and target displacement were collected during the experiment. Since only the initial loading phase was analyzed in this simulation, a simulation including puncture phenomena will be carried out in the near future.

### 4.3. Results and discussion

#### 4.3.1. Needle insertion manipulator

The ultrasound images in Fig. 11(a) show that the inferior vena cava in the liver collapsed from the force put on the needle by the liver tissues during insertion. Finally, the needle tip reached the target in the inferior vena cava (not shown in figure).

Fig. 12 shows the relation between needle displacement and force during the experiment. As can be seen in the figure, there is a nonlinear increase in force (of the liver tissues against the needle) as a function of increased needle displacement (distance traveled by the needle). As also shown in previous work [34,37], Fig. 12 shows that the main puncture event is designated by a peak in

force after a steady rise, followed by a sharp decrease. This data explains that when the needle punctures the liver, the tissues do not respond with a constant force. Instead, the needle first pushes the tissue and then instantaneously punctures it. The first sharp decrease in the graph of Fig. 12 means that the needle punctured the liver membrane, while the second sharp decrease means that the needle punctured the inferior vena cava. In addition, after the experiment, we dissected the liver and confirmed that the needle had punctured the inferior vena cava. Both the ultrasound images and force information verified the accuracy and effectiveness of our needle insertion manipulator.

The material properties of a hard cancer are different from a soft inferior vena cava, which is virtual target of this experiment. Then, we should conduct the experiment, in which the target is a cancer and/or other hard tissue, to validate our manipulator, in future work.

#### 4.3.2. Physical liver model

Fig. 11(b) shows a simulation of the deformation of the liver, which is confirmed by the ultrasound images captured during the in vivo experiment that are shown in Fig. 11(a). In Fig. 11(b), the color

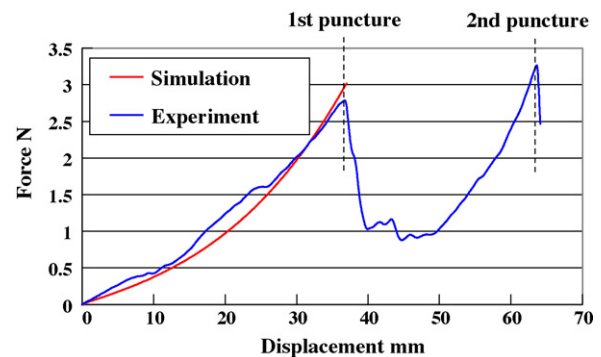


**Fig. 12.** Force as a function of needle displacement. The first sharp decrease in the experimental result means that the needle punctured the liver membrane, while the second sharp decrease means that the needle punctured the inferior vena cava. The simulation result present that the liver model reproduces the relation between needle displacement and force observed in the live liver with high accuracy during only the initial pushing phase.



of each finite element indicates the stress on it. Fig. 12 shows the relation between needle displacement and force for both the real liver of the in vivo experiment and the liver of the simulation model. As is evident in the figure, the liver model we developed reproduces the relation between needle displacement and force observed in the live liver with high accuracy during only the initial pushing phase. In summary, it is strongly suggested from the discussion above that the liver model we developed accurately reproduces the in vivo situation.

However, our validation using this liver shape was not rigorous, because the shape of a real porcine liver is not the same as that of liver model. Therefore, the deformation analysis and evaluation of a liver model with the shape of a real porcine liver should be carried out in the future.

Moreover, only the initial loading phase was analyzed in this numerical simulation. It is necessary to conduct simulation that includes an analysis of the situation in which the needle advances into the liver, so that we provide the further detailed information to a doctor. A simulation including puncture phenomenon will be carried out in the near future.

## 5. Conclusion

The purpose of our research was to develop an integrated robotic system with image guidance and deformation simulation for the purpose of accurate needle insertion. We designed both an ultrasound-guided needle insertion manipulator and a physical model to simulate liver deformation. We carried out an in vivo experiment using a porcine liver to validate the effectiveness of our needle insertion manipulator and liver model. The results of the in vivo experiment showed that the needle insertion manipulator accurately positions the needle tip into the target. The experimental results also showed that the liver model accurately reproduced the nonlinear increase of force upon the needle during insertion. Based on these results, it is suggested that the needle insertion manipulator and physical liver model developed and validated in this work are effective for accurate needle insertion.

In future, further precise organ modeling and validation will be carried out. For example, a modeling based on acquisition of organ geometries using CT or MRI images will be researched for actual applications. In addition, the needle insertion manipulator and physical liver model will be further integrated as a system to achieve safe and precise operation.

## Acknowledgements

This work was supported in part by “Establishment of the Consolidated Research Institute for Advanced Science and Medical Care,” Encouraging Development Strategic Research Centers Program, Special Coordination Funds for Promoting Science and Technology, Ministry of Education, Culture, Sports, Science and Technology, Japan; Global COE (Centers of Excellence) Program “Global Robot Academia,” Waseda University, Tokyo, Japan; and “The robotic medical technology cluster in Gifu prefecture,” Knowledge Cluster Initiative, Ministry of Education, Culture, Sports, Science and Technology, Japan; in part by High-Tech Research Center Project from MEXT (Ministry of Education, Culture, Sports, Science and Technology).

## References

- [1] Curley SA. Radiofrequency ablation of malignant liver tumors. *The Oncologist* 2001;6(1):14–23.
- [2] Shiina S, Teratani T, Obi S, Hamamura K, Koike Y, Omata M. Percutaneous ethanol injection therapy for liver tumors. *European Journal of Ultrasound* 2001;13(2):95–106.
- [3] Daraio P, Hannaford B, Menciassi A. Smart surgical tools and augmenting devices. *IEEE Transactions on Robotics and Automation* 2003;19(5):782–92.
- [4] Taylor RH, Stoianovici D. Medical robotics in computer-integrated surgery. *IEEE Transactions on Robotics and Automation* 2003;19(5):765–81.
- [5] Kazanides P, Fichtinger G, Hager GD, Okamura AM, Whitcomb LL, Taylor RH. Surgical and interventional robotics. *IEEE Robotics & Automation Magazine* 2008;15(2):122–30.
- [6] Fichtinger G, Kazanides P, Okamura AM, Hager GD, Whitcomb LL, Taylor RH. Surgical and interventional robotics: part II. *IEEE Robotics & Automation Magazine* 2008;15(3):94–102.
- [7] Masamune K, Fichtinger G, Patriciu A, Susil RC, Taylor RH, Kavoussi LR, et al. System for robotically assisted percutaneous procedures with computed tomography guidance. *Journal of Computer Aided Surgery* 2001;6(6):370–83.
- [8] Fichtinger G, Deweese TL, Patriciu A, Tanace A, Mazilu D, Anderson JH, et al. System for robotically assisted prostate biopsy and therapy with intraoperative CT guidance. *Academic Radiology* 2002;9(1):60–74.
- [9] Loser MH, Navab N. A new robotic system for visually controlled percutaneous interventions under CT fluoroscopy. *MICCAI 2000*:887–96.
- [10] Yanof J, Haaga J, Klahr P, Bauer C, Nakamoto D, Chaturvedi A, et al. CT-integrated robot for interventional procedures: preliminary experiment and computer–human interfaces. *Journal of Computer Aided Surgery* 2001;6:352–9.
- [11] Masamune K, Ohara F, Matsumiya K, Liao H, Hashizume M, Dohi T. MRI compatible robot for needle placement therapy with accurate registration. In: *Proceedings of world congress on medical physics and biomedical engineering*, vol. 14. 2006. p. 3056–9.
- [12] Hashizume M, Yasunaga T, Tanoue K, Ieiri S, Konishi K, Kishi K, et al. New real-time MR image-guided surgical robotic system for minimally invasive precision surgery. *International Journal of Computer Assisted Radiology and Surgery* 2008;2(6):317–25.
- [13] Krieger A, Susil RC, Ménard C, Coleman JA, Fichtinger G, Atalar E, et al. Design of a novel MRI compatible manipulator for image guided prostate interventions. *IEEE Transactions on Biomedical Engineering* 2005;52(2):306–13.
- [14] Tajima F, Kishi K, Nishizawa K, Kan K, Nemuro Y, Takeda H, et al. A magnetic resonance compatible surgical manipulator: part of a unified support system for the diagnosis and treatment of heart disease. *Advanced Robotics* 2003;17(6):561–75.
- [15] Oura M, Kobayashi Y, Okamoto J, Fujie MG. Development of MRI compatible versatile manipulator for minimally invasive surgery. In: *Proceedings of 2006 IEEE biomedical robotics and biomechanics*. 2006. p. 176–81.
- [16] Hong J, Dohi T, Hashizume M, Konishi K, Hata N. An ultrasound-driven needle-insertion robot for percutaneous cholecystostomy. *Physics in Medicine and Biology* 2004;49:441–55.
- [17] Fichtinger G, Fiene JP, Kennedy CW, Kronreif G, Iordachita I, Song DY, et al. Robotic assistance for ultrasound-guided prostate brachytherapy. *Medical Image Analysis* 2008;12(5):535–45.
- [18] Terayama M, Furusho J, Monden M. Curved multi-tube device for path-error correction in a needle-insertion system. *The International Journal of Medical Robotics and Computer Assisted Surgery* 2007;3:125–34.
- [19] Corrala G, Ibáñez L, Nguyen C, Stoianovici D, Navab N, Cleary K. Robot control by fluoroscopic guidance for minimally invasive spine procedures. In: *Proceedings of the 18th international congress and exhibition of 2004 computer assisted radiology and surgery*. 2004. p. 509–14.
- [20] Famaey N, Sloten JV. Soft tissue modelling for applications in virtual surgery and surgical robotics. *Computer Methods in Biomechanics and Biomedical Engineering* 2008;11(4):351–66.
- [21] The IUPS Physiome Project. <http://www.bioeng.auckland.ac.nz/physiome/physiome.project.php>.
- [22] Miller K. Constitutive modelling of abdominal organs. *Journal of Biomechanics* 2000;33(3):367–73.
- [23] Miller K, Chinzei K, Orsengo G, Bednars P. Mechanical properties of brain tissue in vivo: experiment and computer simulation. *Journal of Biomechanics* 2000;33:1369–76.
- [24] Tillier Y, Paccini A, Durand-Reville M, Bay F, Chenot JL. Three-dimensional finite element modeling for soft tissues surgery. *Computer Assisted Radiology and Surgery* 2003;349–55.
- [25] Alterovitz R, Lim A, Goldberg K, Chirikjian GS, Okamura AM. Steering flexible needles under markov motion uncertainty. In: *2005 IEEE international conference on intelligent robots and systems*. 2005. p. 120–5.
- [26] Alterovitz R, Goldberg K, Okamura A. Planning for steerable bevel-tip needle insertion through 2D soft tissue with obstacles. In: *2005 IEEE international conference on robotics and automation*. 2005. p. 1652–7.
- [27] DiMaio SP, Salcudean SE. Needle insertion modelling and simulation. *IEEE Transactions on Robotics and automation* 2003;19(5):864–75.
- [28] DiMaio SP, Salcudean SE. Interactive simulation of needle insertion model. *IEEE Transactions on Biomedical Engineering* 2005;52(7):1167–79.
- [29] Sakuma I, Nishimura Y, Chui CK, Kobayashi E, Inada H, Chen X, et al. In vitro measurement of mechanical properties of liver tissue under compression and elongation using a new test piece holding method with surgical glue. In: *Proceedings on international symposium IS4TM*. 2003. p. 284–92.
- [30] Chui C, Kobayashi E, Chen X, Hisada T, Sakuma I. Combined compression and elongation experiments and non-linear modelling of liver tissue for surgical simulation. *Medical and Biological Engineering and Computing* 2006;42(6):787–98.

- [31] Goksel O, Salcudean SE, DiMaio SP, Rohling R, Morris J. 3D Needle–tissue interaction simulation for prostate brachytherapy. *Medical Image Computing and Computer-Assisted Intervention* 2005;827–34.
- [32] Dehghan E, Salcudean SE. Needle insertion point and orientation optimization in non-linear tissue with application to brachytherapy. In: 2007 IEEE international conference on robotics and automation. 2007. p. 2267–72.
- [33] Schwartz JM, Denninger M, Rancourt D, Moisan C, Laurendeau D. Modelling liver tissue properties using a non-linear visco-elastic model for surgery simulation. *Medical Image Analysis* 2005;9(2):103–12.
- [34] Okamura AM, Simone C, O'Leary MD. Force modeling for needle insertion into soft tissue. *IEEE Transactions on Biomedical Engineering* 2004;51(10):1707–16.
- [35] Heverly M, Dupont P, Friedman J. Trajectory optimization for dynamic needle insertion. In: IEEE international conference on robotics and automation. 2005. p. 1646–51.
- [36] Kobayashi Y, Okamoto J, Fujie MG. Physical properties of the liver for needle insertion control. In: 2004 IEEE international conference on intelligent robotics and systems. 2004. p. 2960–6.
- [37] Kobayashi Y, Okamoto J, Fujie MG. Physical properties of the liver and the development of an intelligent manipulator for needle insertion. In: 2005 IEEE international conference on robotics and automation. 2005. p. 1644–51.
- [38] Kobayashi Y, Onishi A, Hoshi T, Kawamura K, Fujie MG. Deformation simulation using a viscoelastic and nonlinear organ model for control of a needle insertion manipulator. In: 2007 IEEE international conference on intelligent robotics and systems. 2007. p. 1801–8.
- [39] Kobayashi Y, Onishi A, Hoshi T, Kawamura K, Fujie MG. In vitro validation of a viscoelastic and nonlinear liver model for needle insertion. In: Proceedings of 2008 IEEE biomedical robotics and biomechatronics. 2008. p. 469–76.
- [40] Kobayashi Y, Onishi A, Hoshi T, Kawamura K, Hashizume M, Fujie MG. Development and validation of a viscoelastic and nonlinear liver model for needle insertion. *International Journal of Computer Assisted Radiology and Surgery* 2009;4(1):53–63.
- [41] Hong J, Nakashima H, Konishi K, Ieiri S, Tanoue K, Nakamura M, et al. Interventional navigation for abdominal therapy based on simultaneous use of MRI and ultrasound. *Medical and Biological Engineering and Computing* 2006;44(12):1127–34.
- [42] Zienkiewicz OC, Cheung YK. The finite element method in structural and continuum mechanics. McGraw-Hill Publ. Co.; 1967.
- [43] Ma C, Hori Y. The application of fractional order control to backlash vibration suppression. In: Proceedings of American control conference. 2004. p. 2901–6.

**Yo Kobayashi** was born in Japan in 1981. He received the BS and MS degree from graduate school of science and engineering, Waseda University, Japan in 2004 and 2005, and the PhD degree in engineering from Waseda University, 2008. He was Visiting Research Associate, Graduate school of Science and Engineering, Waseda University from 2005 to 2006. He was Japan Society for the Promotion of Science (JSPS) Research Fellowship for Young Scientists during 2007. He was Research Associate, Institute for Biomedical Engineering, Waseda University during 2008. Since 2009, he was Research Associate, Faculty of Science and Engineering, Waseda University. He is also a member of IEEE, the Japan Society of Computer-Aided Surgery. His current research interests include computer-aided surgery (CAS), surgical simulation, and medical robot.

**Akinori Onishi** was born in Japan in 1983. He received the BS and MD degree from graduate school of science and engineering, Waseda University, Japan in 2006 and 2008.

**Hiroki Watanabe** was born in Japan in 1985. He received the BS degree from graduate school of science and engineering, Waseda University, Japan in 2008. He is also a member of IEEE, the Japan Society of Computer-Aided Surgery. His current research interests include computer-aided surgery, organ modeling, and surgical simulation.

**Takeharu Hoshi** received his BS and MS degrees in mechanical engineering from Waseda University. He is currently a PhD candidate at Waseda University and a research associate. His research interests include mechanical modeling of soft biological tissues, identification of individual properties, and simulation based surgical robot motion planning.

**Kazuya Kawamura** was born in Japan in 1982. He received the BS and MS degree from Graduate School of Science and Engineering, Waseda University, Japan in 2004 and 2006, and the PhD degree in engineering from Waseda University, 2009. He was Visiting Research Associate (COE program), Graduate School of Science and Engineering, Waseda University from 2006 to 2008 and Visiting Research Associate (Global COE program), Graduate School of Science and Engineering, Waseda University from 2008 to 2009. Since 2009, he was Research Associate, Faculty of Science and Engineering, Waseda University. He is also a member of the Robot Society of Japan, the Japan Society of Computer-Aided Surgery. His current research interests include computer-aided surgery (CAS), surgical simulation, and robotic tele-surgery.

**Makoto Hashizume** was born in Japan in 1953. He received the MD degree from the School of Medicine, Kyushu University, Fukuoka, Japan, in 1979, and the PhD degree in medical science from Kyushu University, in 1984. From 1990 to 1997, he was an Assistant Professor in the Department of Surgery and Science, Faculty of Medical Sciences, Kyushu University, where he was an Associate Professor during 1998 and has been a Professor in the Department of Advanced Medical Initiatives, Faculty of Medical Sciences, since 1999. Since 2006, he has also been the Director of Emergency and Critical Care Center, and the Training Center for Endoscopic Surgery, Kyushu University Hospital. His current research interests include surgical robot, image-guided surgery, endoscopic surgery, and emergency medicine. Prof. Hashizume is a member of the Fellow of American College of Surgeons (FACS), the Society of American Gastrointestinal Endoscopic Surgeons, the International Society of Computer-Aided Surgery, the Japan Surgical Society, and the Japanese Society for Emergency Medicine. He is a member of the Editorial Boards of several journals including the Journal of Robotic Surgery, International Journal of Computer Assisted Radiology and Surgery (CARS), Surgery Today.

**Masakatsu G. Fujie** was born in Japan in 1945. He received MS degree from Graduate School of Science and Engineering, Waseda University, Japan in 1971 and in PhD degree in Engineering, Waseda University, Tokyo, Japan in 1999. He worked the Mechanical Engineering Research Laboratory, Hitachi Ltd from 1971 to 2000 where he was Senior Researcher at the Mechanical Engineering Research Laboratory, Hitachi Ltd since 1984 and Principle Researcher and Project Leader for “eMedical and Welfare Apparatus Development Project” at the Mechanical Engineering Research Laboratory, Hitachi Ltd. since 1995. He also was Head of researchers at the Mechanical Engineering Research Laboratory, Hitachi Ltd. and director of the Medical and Welfare Apparatus Development research laboratory since 1999. Since 2001, he was Professor at Faculty of Science and Engineering, Waseda University. His current research interests include surgical robot, image-guided surgery, endoscopic surgery, and assistive robot. Prof. Fujie is also a member of IEEE, the International Society of Computer-Aided Surgery, the Japan Surgical Society.